Supplementary Materials for

"Strengthened impact of boreal winter North Pacific Oscillation on ENSO development in warming climate"

Shangfeng Chen[1], Wen Chen[2,3*], Shang-Ping Xie[4] , Bin Yu[5], Renguang Wu[6], Zhibiao Wang[1], Xiaoqing Lan[1], and Hans-F Graf[7]

[1]*Center for Monsoon System Research, Institute of Atmospheric Physics, Chinese Academy of Sciences, Beijing, China*

[2]*Yunnan Key Laboratory of Meteorological Disasters and Climate Resources in the Greater Mekong Subregion, Yunnan University, Kunming, China*

[3]*Department of Atmospheric Sciences, Yunnan University, Kunming 650500, China*

[4]*Scripps Institution of Oceanography, University of California, San Diego, La Jolla, California*

[5]*Climate Research Division, Environment and Climate Change Canada, Toronto, ON, Canada*

[6]*School of Earth Sciences, Zhejiang University, Hangzhou, China*

[7]*Center for Atmospheric Science, University of Cambridge, Cambridge, UK*

npj Climate and Atmospheric Science

Corresponding author*:

Dr. Wen Chen

Department of Atmospheric Sciences, Yunnan University, Kunming 650500, China

e-mail: chenwen-dq@ynu.edu.cn

This PDF file includes:

Figs. S1 to S18

Table S1

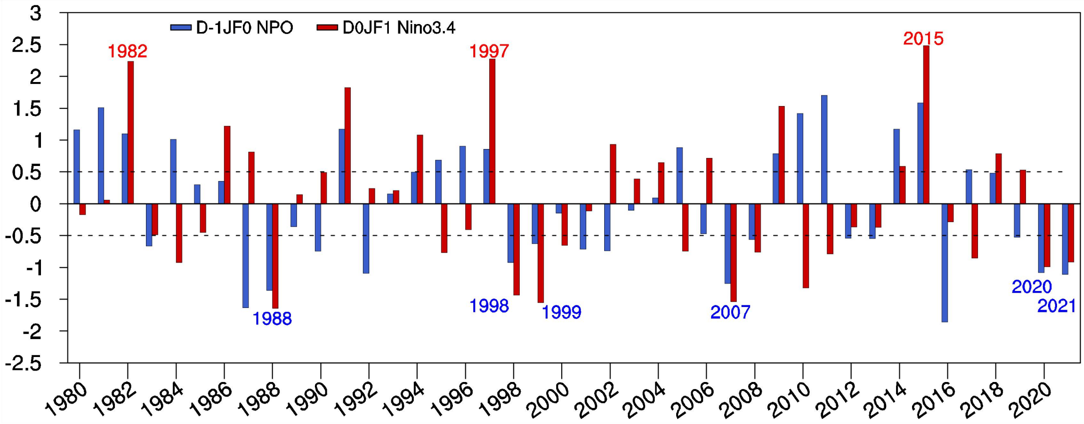

Supplementary Figure 1. Observed NPO and Niño3.4 SST indices. Observed normalized D-1JF0 NPO index (blue bars) and the D0JF1 Niño3.4 SST index (red bars). Years in *X*-axis are labeled according to the D-1JF0 NPO index.

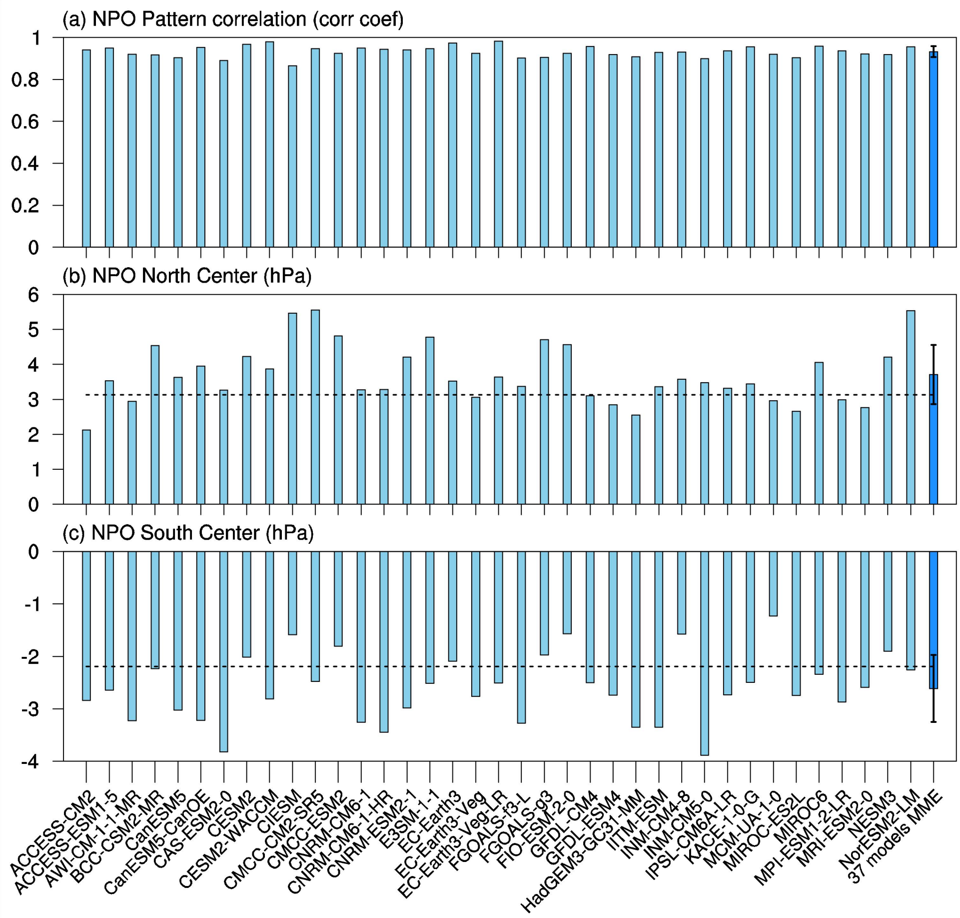

Supplementary Figure 2. Assessment of NPO simulation in CMIP6 models. (a) Pattern correlations of the NPO-related D-1JF0 SLP anomalies (obtained by regression upon on the normalized D-1JF0 NPO index) over North Pacific (20^{o}-70^{o}N and 120^{o}E-100^{o}W) between observations and the 37 CMIP6 models (light blue bars). (b) Intensity of the NPO's northern lobe measured by D-1JF0 SLP anomalies (hPa) regressed on the normalized D-1JF0 NPO index averaged over 50^{o}-80^{o}N and 160^{o}E-120^{o}W. (c) Intensity of the NPO's southern lobe measured by D-1JF0 SLP anomalies (hPa) regressed on the normalized D-1JF0 NPO index averaged over 20^{o}-45^{o}N and 150^{o}E-130^{o}W. Multi-model mean (MME) for the 37 models (dark blue bar) is also shown in (a)-(c), with error bars indicating the inter-model standard deviation.

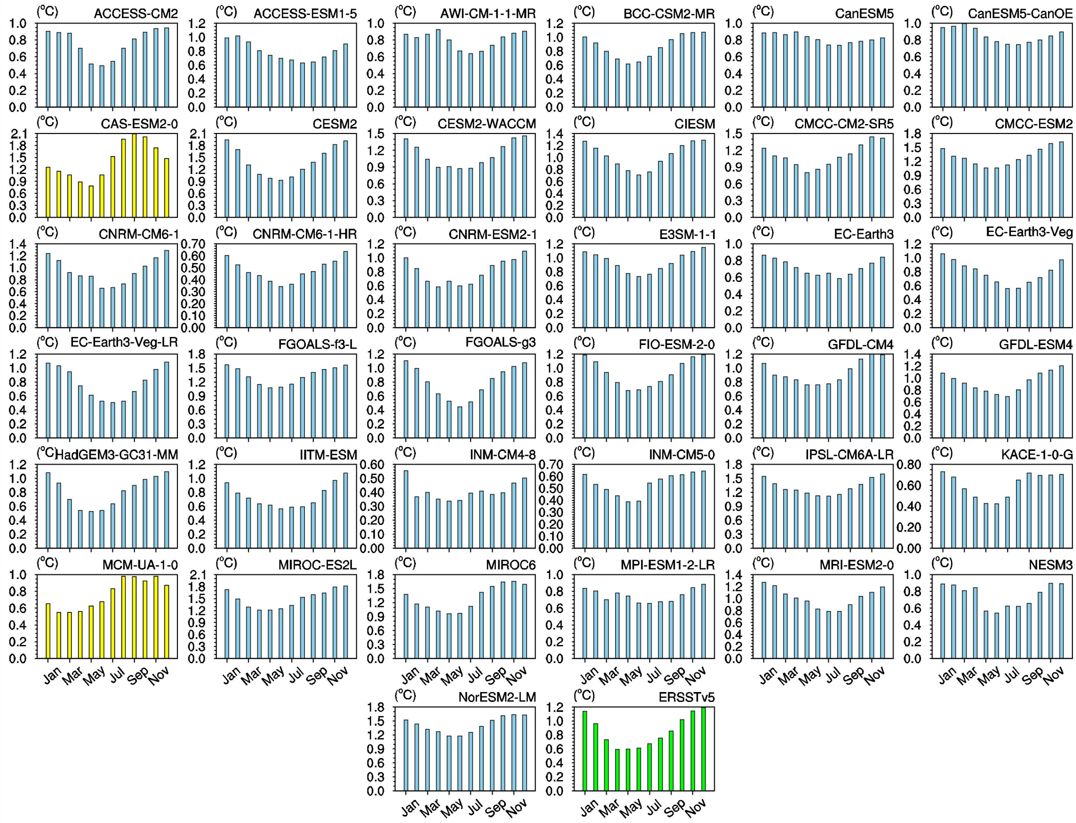

Supplementary Figure 3. Assessment of ENSO phase locking simulation in CMIP6 models. Standard deviation (°C) of the monthly Niño3.4 SST index in the 37 CMIP6 models for the present-day climate period of 1900-1990 and in the ERSSTv5 over period of 1949-2021. Except the CAS-ESM2-0 and MCM-UA-1-0 (yellow bars), other 35 CMIP6 models (light blue bars) can generally well produce the observed (green bars) winter phase locking feature of ENSO.

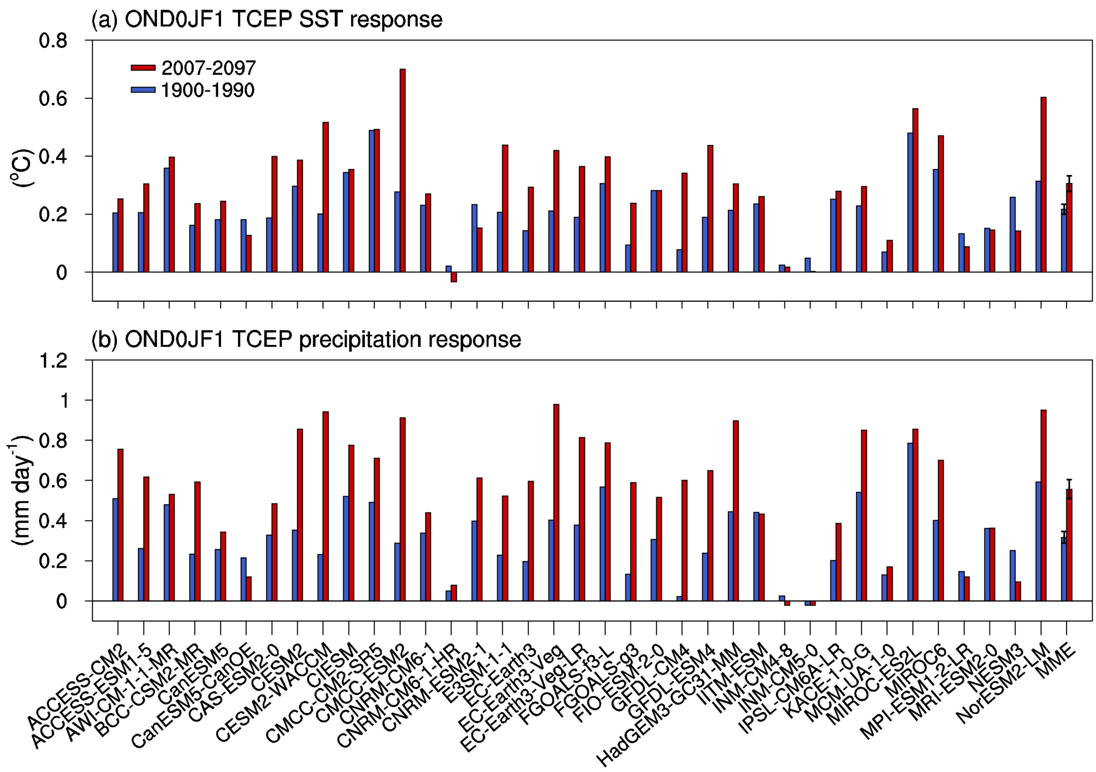

Supplementary Figure 4. Stronger impact of winter NPO on the following winter ENSO under global warming. As in Fig. 2a and Fig. 2b, but all the 37 CMIP6 models are used.

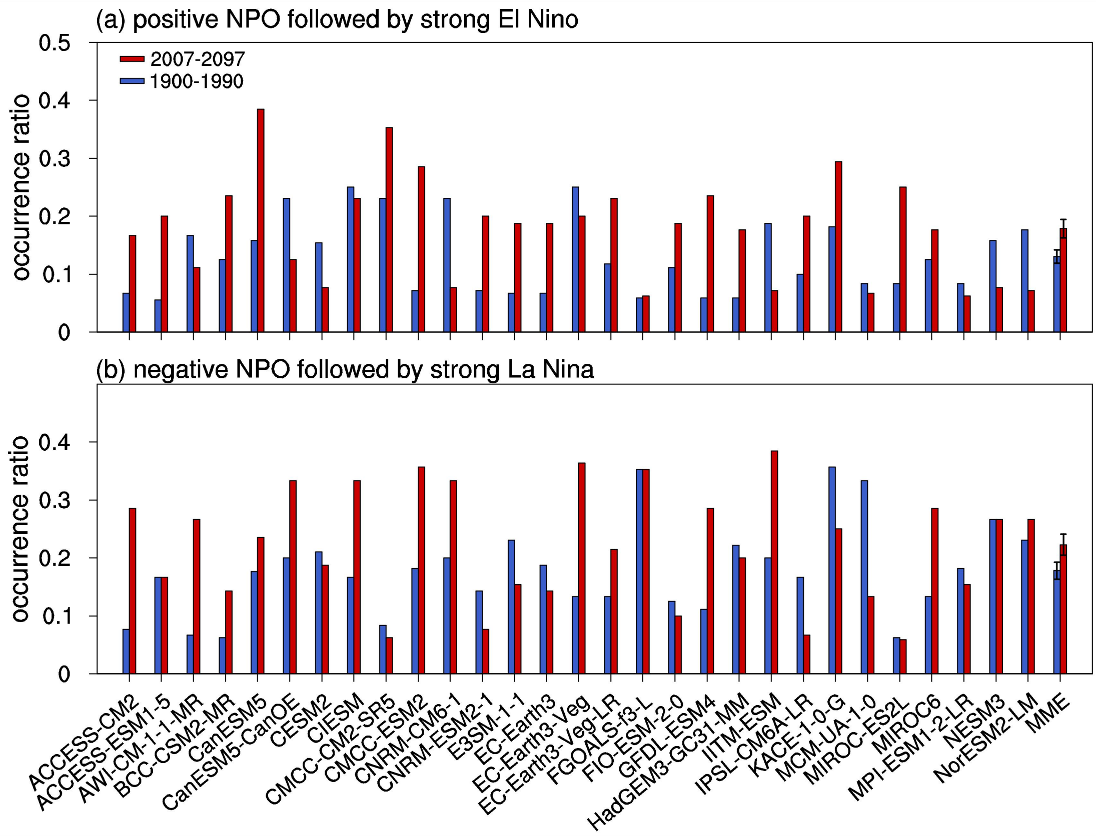

Supplementary Figure 5. Increased frequency of winter NPO events followed by strong ENSO events under global warming. As in Fig. 3a and 3b, but for a comparison of the occurrence ratio of (a) positive winter NPO events (D-1JF0 NPO index larger than 1.0 s.d.) followed by strong El Niño events in the following winter (D0JF1 Niño3.4 SST index larger than 1.5 s.d.) over the total positive NPO events, and (b) negative NPO events (D-1JF0 NPO index smaller than -1.0 s.d.) followed by strong La Niña events (D0JF1 Niño3.4 SST index smaller than 1.5 s.d.) over the total negative NPO events for the present-day climate period (blue bars) and the future climate period (red bars) in the 29 models.

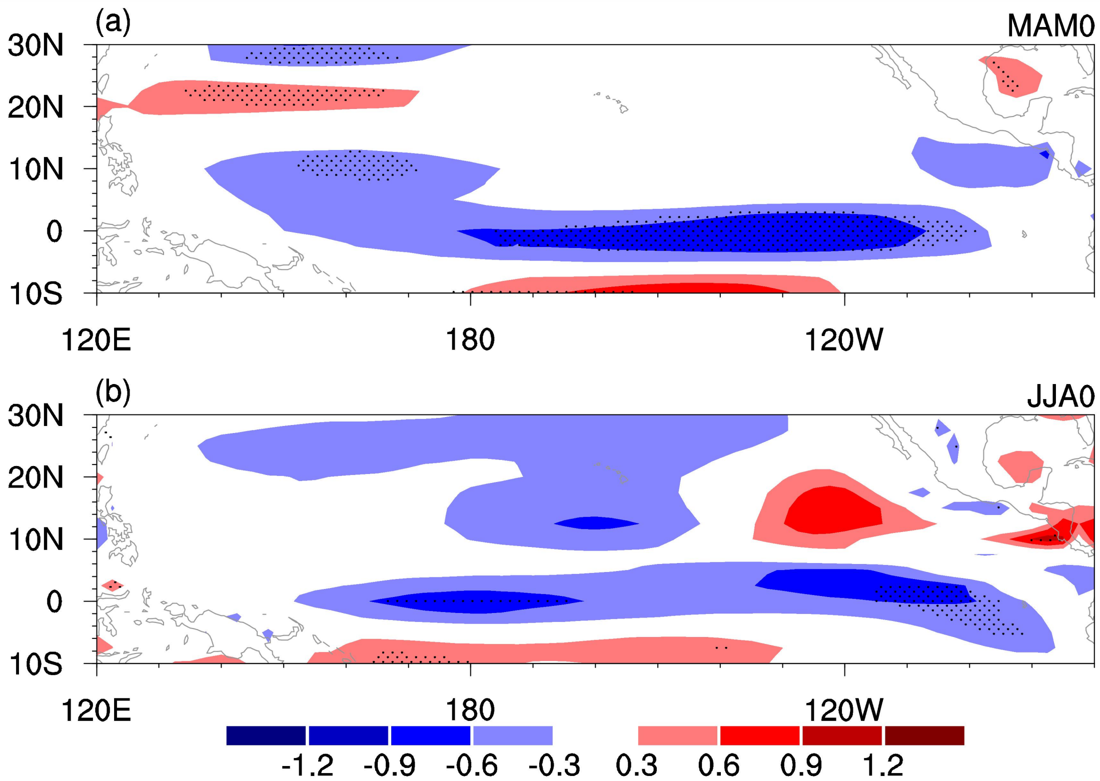

Supplementary Figure 6. Background mean surface wind speed change under global warming. Multi-model mean change of surface wind speed (m s^{-1}) in (a) MAM0, and (b) JJA0 between the future and present-day climate periods using the 29 selected CMIP6 models. Stippling regions indicate differences that are significant at the 95% confidence level according to the two-tailed Student's *t* test.

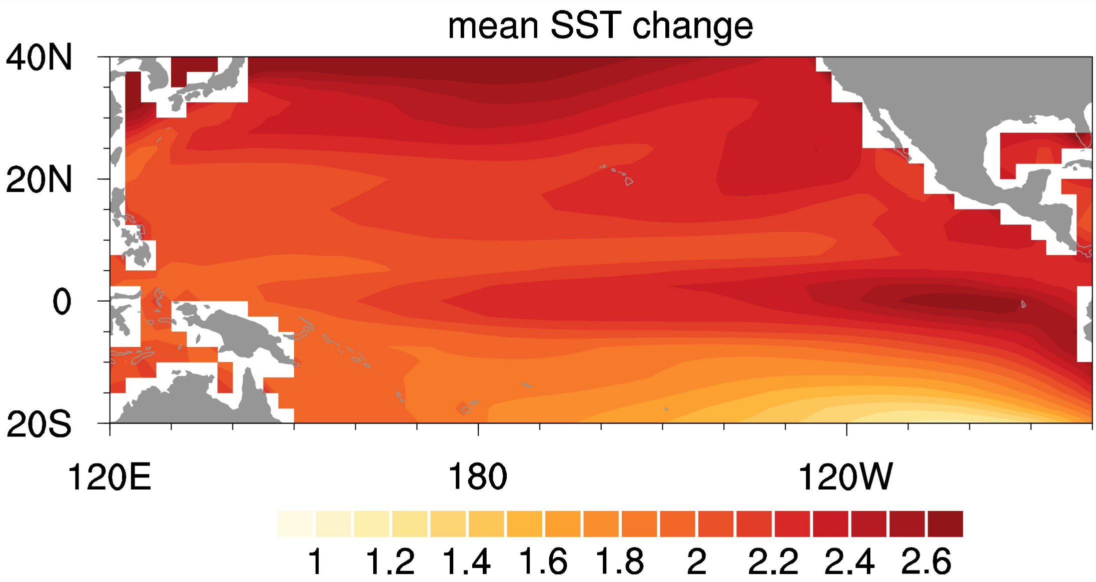

Supplementary Figure 7. Increase in background mean SST under global warming. Multi-model mean change of SST (°C) between the future and present-day climate periods using the 29 selected CMIP6 models.

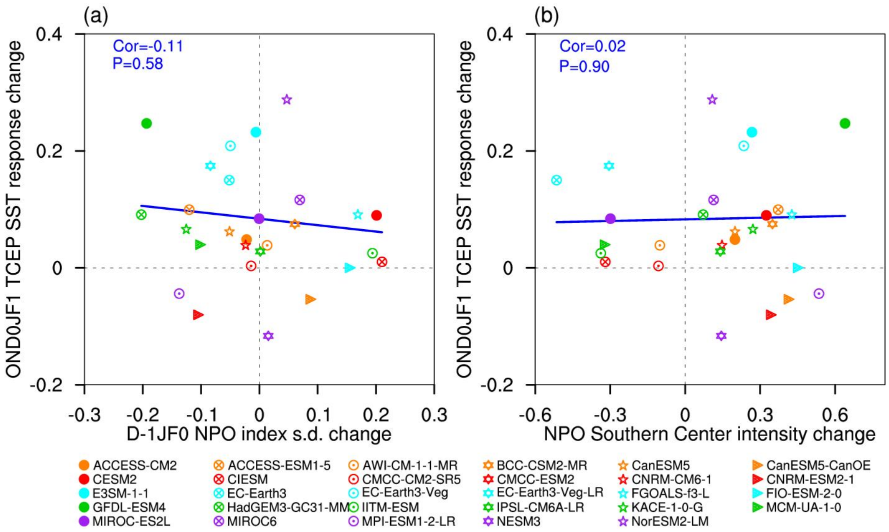

Supplementary Figure 8. Little impact from changing NPO variability, southern center of NPO and trade wind charging process. Inter-model relationship between the change (future minus present-day) of the OND0JF1 TCEP SST response to D-1JF0 NPO (*Y*-axis, ^{o}C) with (a) the change of the standard deviation of the D-1JF0 NPO index (*X*-axis), and (b) with the change of the intensity of the D-1JF0 NPO's southern lobe (*X*-axis, hPa) among the 29 selected models. Intensity of the NPO's southern lobe is measured by D-1JF0 SLP anomalies (hPa) regressed on the normalized D-1JF0 NPO index averaged over 20^{o}-45^{o}N and 150^{o}E-130^{o}W. Linear fit (blue line) and the statistical property (including the correlation coefficient and *P* value, blue text) are also shown in (a)-(b).

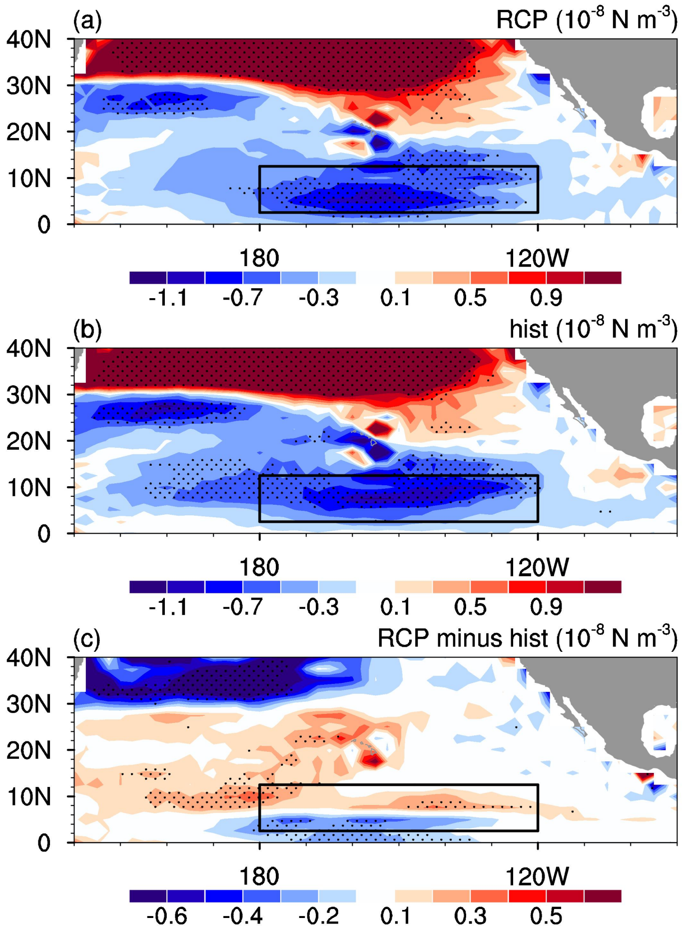

Supplementary Figure 9. Trade wind charging mechanism induced by the NPO and its change under global warming. Regression maps of surface wind curl anomalies (10^{-8} N m^{-3}) in D-1JFM0 onto the normalized D-1JF0 NPO index over the (a) future climate period and (b) the present-day climate period for the MME of the 29 CMIP6 models. (c) is the change of the D-1JFM0 surface wind curl response (10^{-8} N m^{-3}) between the future climate and present-day climate periods. Stippling regions in (a)-(b) indicate the MME of surface wind curl anomalies exceeds 1.0 s.d. of the inter-model variation. Stippling regions in (c) denote the changes that are significant at the 95% confidence level.

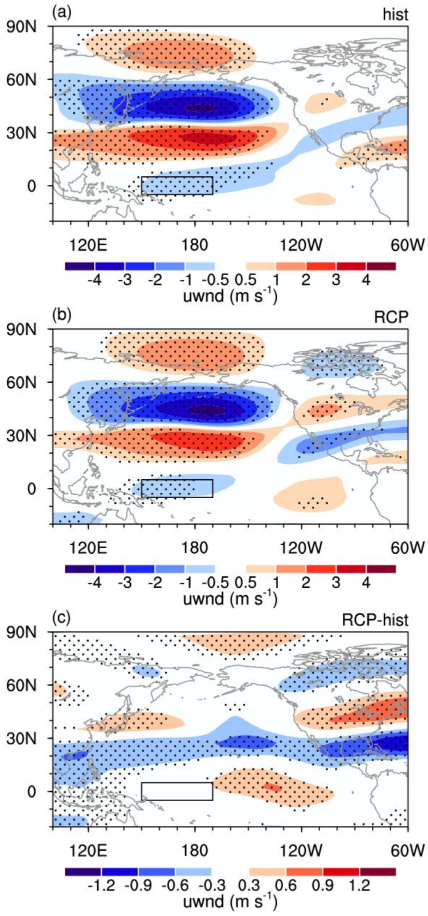

Supplementary Figure 10. Upper tropospheric process induced by the NPO and its change under global warming. Regression map of the 200-hPa zonal wind anomalies (m s^{-1}) in D-1JF0 onto the normalized D-1JF0 NPO index for the MME of the 29 selected models over (a) the present-day period of 1900-1990 and (b) the future climate period of 2007-2097. (c) is the difference between (b) and (a). Stippling regions in (a)-(b) indicate zonal wind anomalies significant at the 95% confidence level. Stippling regions in (c) indicate zonal wind difference significant at the 95% confidence level.

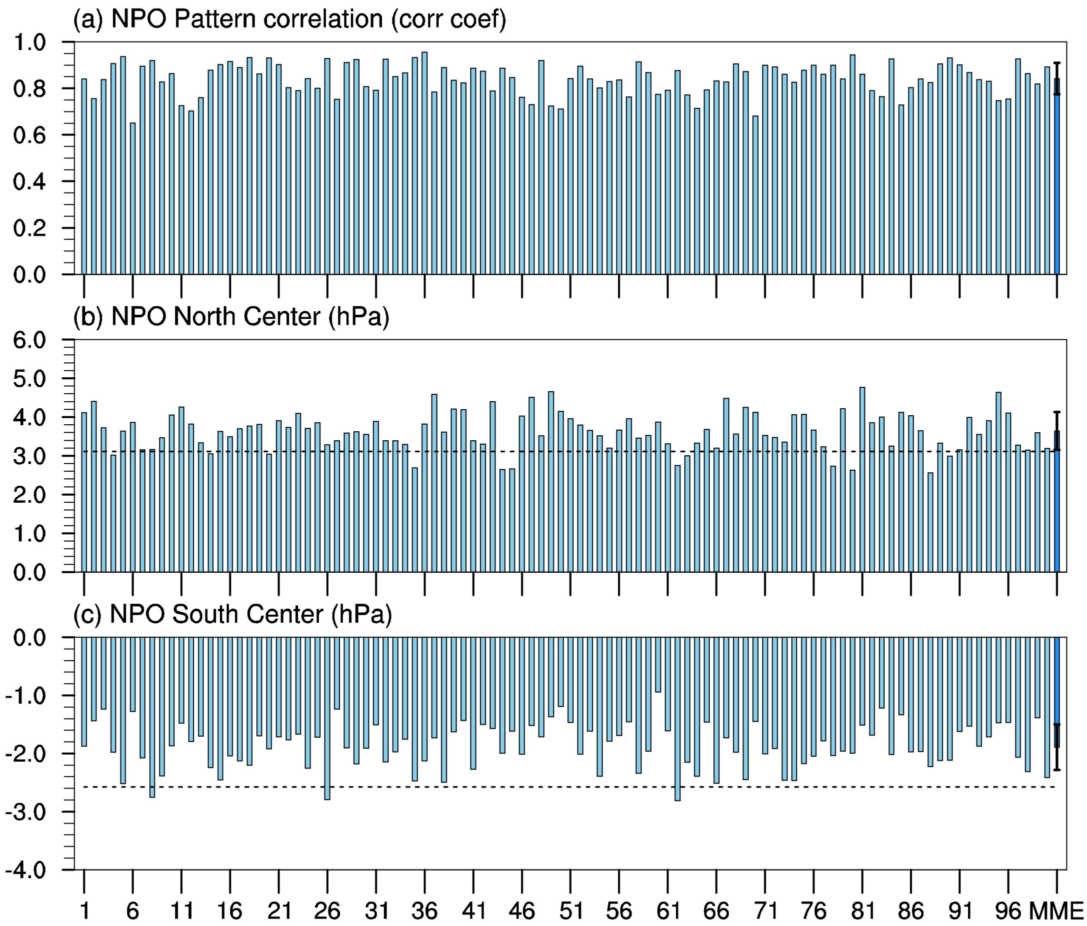

Supplementary Figure 11. Assessment of NPO simulation in large ensemble experiment of MPI-ESM. (a) Pattern correlations of the D-1JF0 SLP anomalies (obtained by regression upon on the normalized D-1JF0 NPO index) over North Pacific (20^{o}-70^{o}N and 120^{o}E-100^{o}W) between observations and the 100-member large ensemble simulations of the MPI-ESM (light blue bars). (b) Intensity of the NPO's northern lobe measured by D-1JF0 SLP anomalies (hPa) regressed on the normalized D-1JF0 NPO index averaged over 50^{o}-80^{o}N and 160^{o}E-120^{o}W. (c) Intensity of the NPO's southern lobe measured by D-1JF0 SLP anomalies (hPa) regressed on the normalized D-1JF0 NPO index averaged over 20^{o}-45^{o}N and 150^{o}E-130^{o}W. Multi-member means are also shown in (a)-(c), with error bars indicating the inter-member standard deviation.

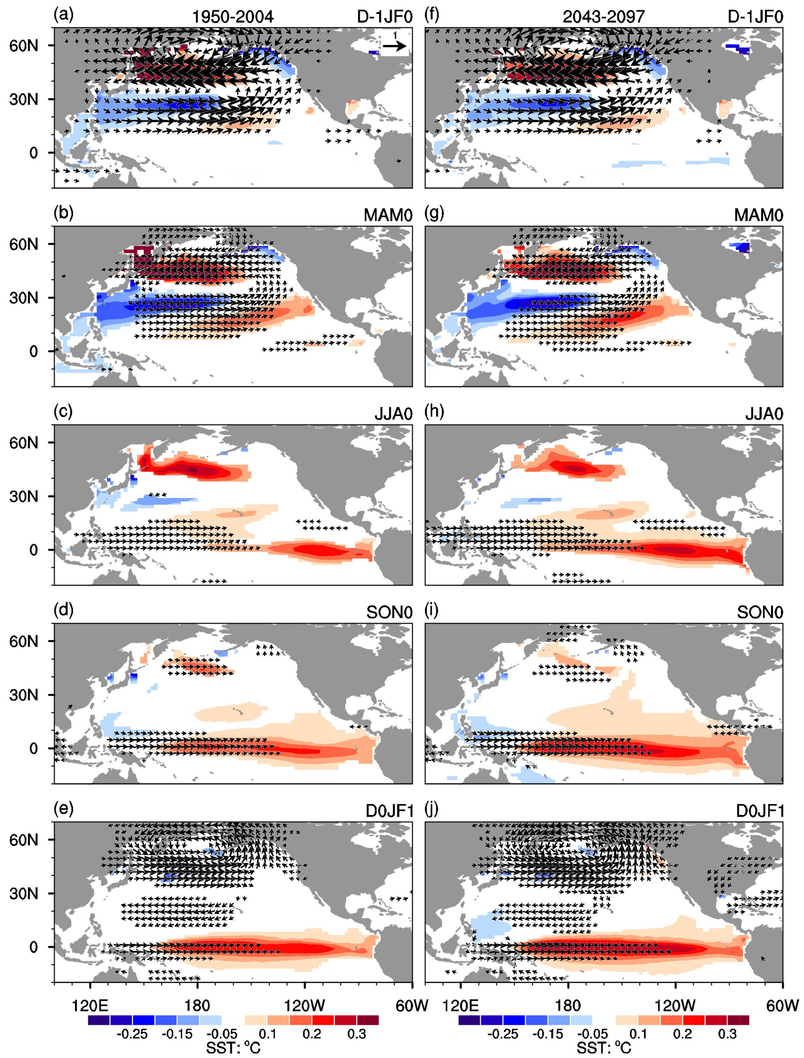

Supplementary Figure 12. Evolutions of winter NPO-related SST and winds anomalies in MPI-ESM. Regression maps of the SST (°C) and 850-hPa wind (m s^{-1}) anomalies in D-1JF0 (b), MAM0 (c), JJA0 (d), SON0 (e) and D0JF1 (f) onto the normalized D-1JF0 NPO index for the MME of the MPI-ESM 100 members over the present-day climate period of 1950-2004. (f)-(j) As in (a)-(e), but for the ensemble mean over the future climate period of 2043-2097. Only MME of SST anomalies exceeds 1.0 s.d. of the inter-member variation is shown.

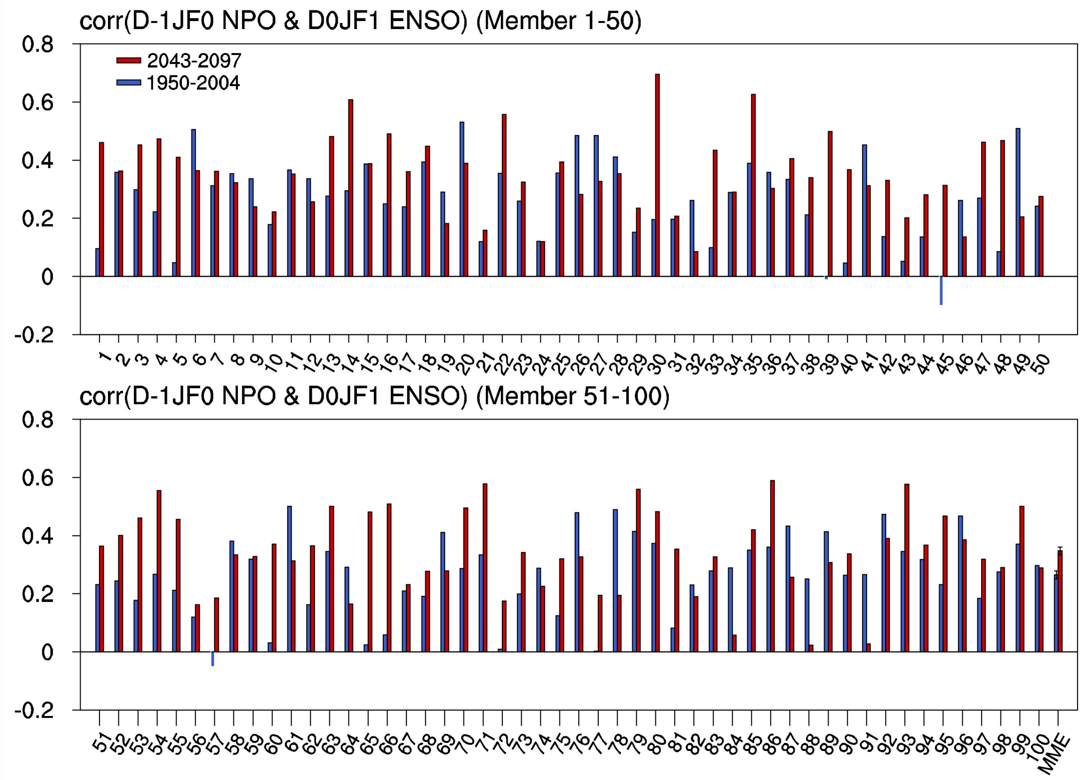

Supplementary Figure 13. Enhanced correlation of winter NPO with the following winter ENSO in MPI-ESM. Correlation coefficient between D-1JF0 NPO index and the OND0JF1 Niño3.4 SST index over the present-day climate period (blue bars) and the future climate period (red bars) in the 100 members large ensemble simulations of the MPI-ESM. MME of the 100 members and the corresponding error bars are also shown. Error bars denote one s.d. of 10000 inter-realizations of the bootstrap test for the present-day and future climate periods.

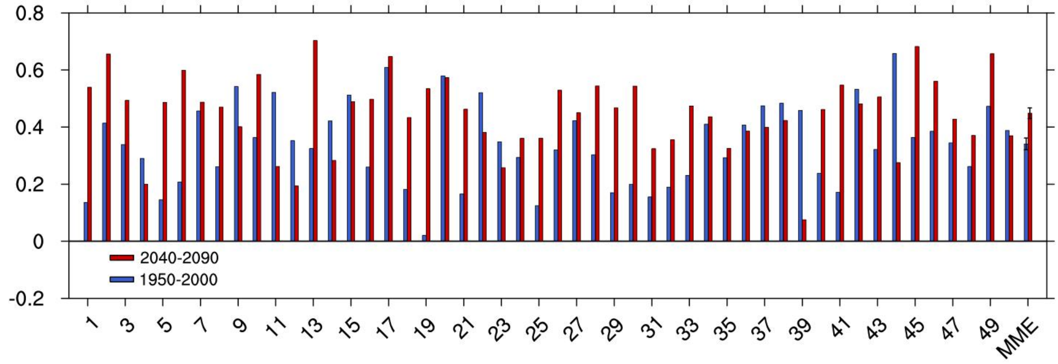

Supplementary Figure 14. Enhanced correlation of winter NPO with the following winter ENSO in CanESM2. Correlation coefficient between D-1JF0 NPO index and the OND0JF1 Niño3.4 SST index over the present-day climate period (blue bars) and the future climate period (red bars) in the 50 members large ensemble simulations of the CanESM2. MME of the 50 members and the corresponding error bars are also shown. Error bars denote one s.d. of 10000 inter-realizations of the bootstrap test for the present-day and future climate periods.

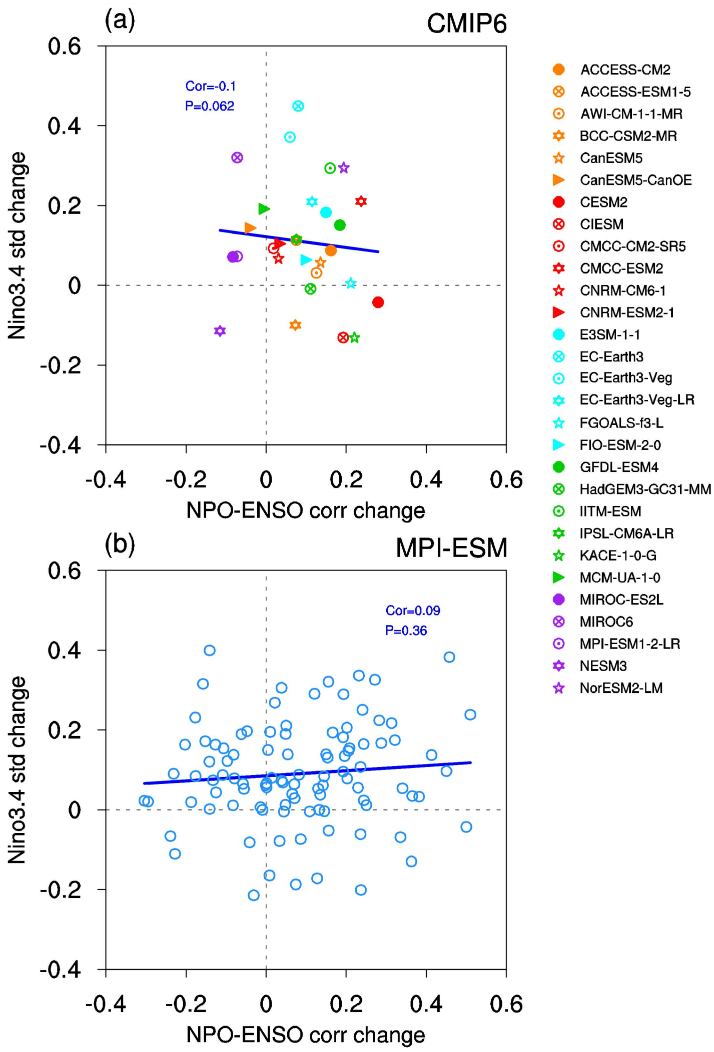

Supplementary Figure 15. Little impact from changing ENSO variability. (a) Inter-model relationship between the change (future minus present-day) of the correlation between D-1JF0 NPO and OND0JF1 ENSO (*X*-axis) with (a) the change of the standard deviation of the OND0JF1 Niño3.4 SST index (*Y*-axis) among the 29 selected models. (b) Inter-member relationship between the change (future minus present-day) of the correlation coefficient between D-1JF0 NPO and OND0JF1 ENSO (*X*-axis) with (a) the change of the standard deviation of the OND0JF1 Niño3.4 SST index (*Y*-axis) among the MPI-ESM 100 members.

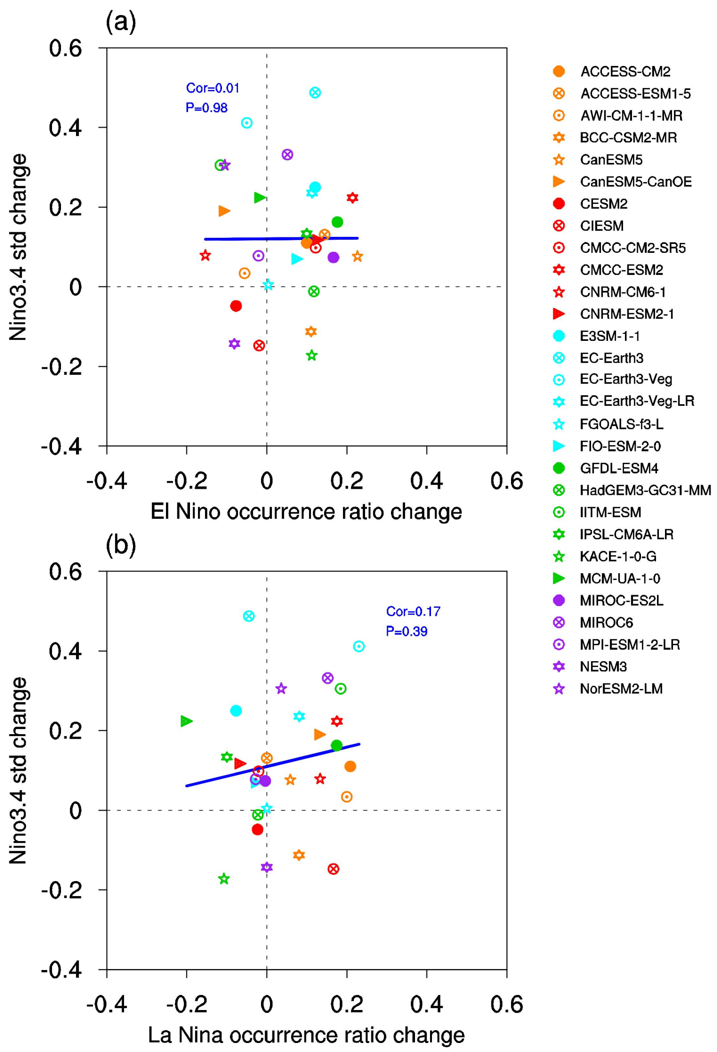

Supplementary Figure 16. Little impact of ENSO variability on the change of the occurrence ratio of NPO events followed by ENSO events. (a) Inter-model relationship between the change (future minus present-day) of the standard deviation of the OND0JF1 Niño3.4 SST index (*Y*-axis) (a) with the change of the occurrence ratio of positive winter NPO events followed by strong El Niño events in the following winter (*X*-axis), and (b) with the change of the occurrence ratio of negative winter NPO events followed by strong La Niña events in the following winter (*X*-axis) among the 29 selected models.

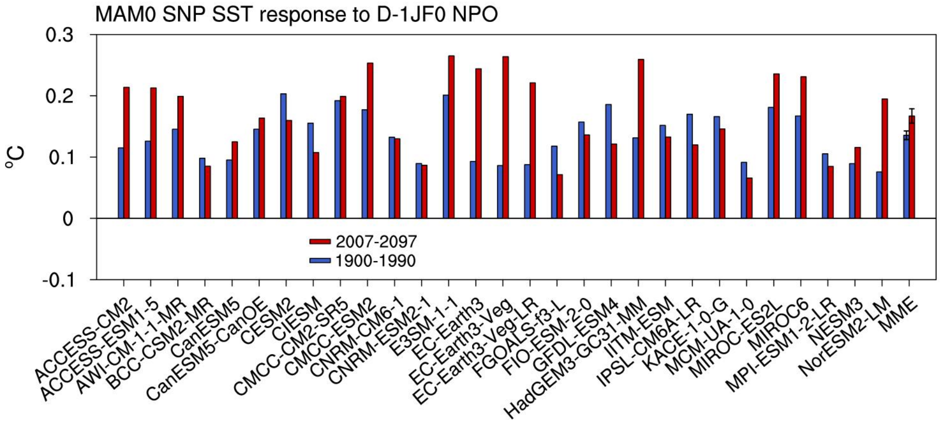

Supplementary Figure 17. Enhaned impact of winter NPO on spring PMM. SST anomalies in MAM0 averaged over the region of 5°-20°N, 180°E-130°W regressed upon the normalized D-1JF0 NPO index over the present-day (blue bar) and the future climate period (red bar) in the 29 models. Multi-model mean (MME) of the 29 models is also shown, with error bars representing 1.0 s.d. of the 10,000 inter-realizations of the bootstrap test.

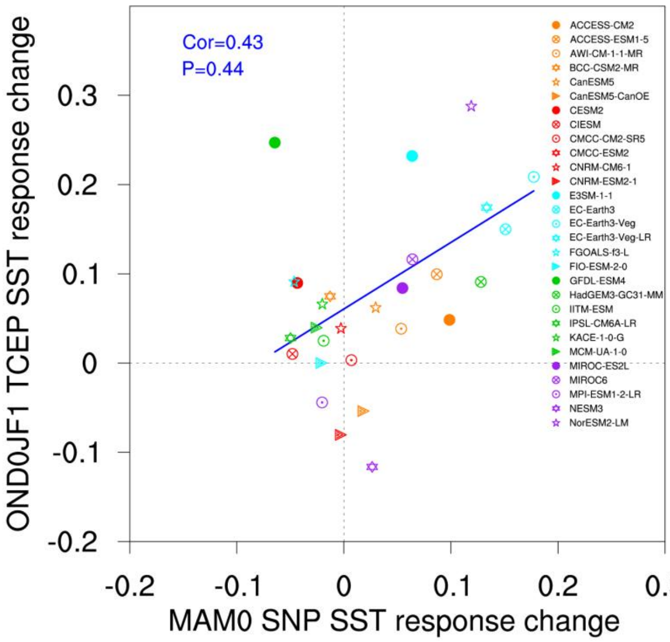

Supplementary Figure 18. Close relation of the change in the winter NPO-ENSO connection with the change in the winter NPO-PMM connection. Inter-model relation between the change (future minus present-day) of the OND0JF1 TCEP SST response to D-1JF0 NPO (*Y*-axis, ^{o}C) with (a) the change of the MAM0 SST anomalies in the subtropical North Pacific (5^{o}-20^{o}N and 180^{o}E-130^{o}W) response to D-1JF0 NPO (*X*-axis, ^{o}C) among the 29 CMIP6 models. Linear fit (blue line) and the statistical property (including the correlation coefficient and *P* value, blue text) are also shown.

Supplementary Table 1. **Information of CMIP6 models employed in this study.** Names of CMIP6 models, the related countries and institutions, their ensemble members used in this study (mostly r1i1p1f1).

Abbr. Name	Institute	Country	Ensemble
ACCESS-CM2	CSIRO	Australia	r1i1p1f1
ACCESS-ESM1-5	CSIRO	Australia	r1i1p1f1
AWI-CM-1-1-MR	AWI	Germany	r1i1p1f1
BCC-CSM2-MR	BCC	China	r1i1p1f1
CanESM5	CCCma	Canada	r1i1p1f1
CanESM5-CanOE	CCCma	Canada	r1i1p2f1
CAS-ESM2-0	CAS	China	r1i1p1f1
CESM2	NCAR	USA	rii1p1f1
CESM2-WACCM	NCAR	USA	r1i1p1f1
CIESM	Tsinghua University	China	r1i1p1f1
CMCC-CM2-SR5	CMCC	Italy	r1i1p1f1
CMCC-ESM2	CMCC	Italy	r1i1p1f1
CNRM-CM6-1	CNRM	France	r1i1p1f2
CNRM-CM6-1-HR	CNRM	France	r1i1p1f2
CNRM-ESM2-1	CNRM	France	r1i1p1f2
E3SM-1-1	DOE	USA	r1i1p1f1
EC-Earth3	Europe consortium	Europe consortium	r1i1p1f1
EC-Earth3-Veg	Europe consortium	Europe consortium	r1i1p1f1
EC-Earth3-Veg-LR	Europe consortium	Europe consortium	r1i1p1f1
FGOALS-f3-L	CAS	China	r1i1p1f1
FGOALS-g3	CAS	China	r1i1p1f1
FIO-ESM-2-0	FIO	China	r1i1p1f1
GFDL-CM4	NOAA, GFDL	USA	r1i1p1f1
GFDL-ESM4	NOAA, GFDL	USA	r1i1p1f1
HadGEM3-GC31-MM	MOHC	UK	r1i1p1f3
IITM-ESM	CCCR-IITM	India	r1i1p1f1
INM-CM4-8	INM	Russia	r1i1p1f1
INM-CM5-0	INM	Russia	r1i1p1f1
IPSL-CM6A-LR	IPSL	France	r1i1p1f1
KACE-1-0-G	NIMS-KMA	Korea	r1i1p1f1
MCM-UA-1-0	UA	USA	r1i1p1f2
MIROC-ES2L	JAMSTEC	Japan	r1i1p1f2
MIROC6	JAMSTEC	Japan	r1i1p1f1
MPI-ESM1-2-LR	MPI-M	Germany	r1i1p1f1
MRI-ESM2-0	MRI	Japan	r1i1p1f1
NESM3	NUIST	China	r1i1p1f1
NorESM2-LM	NCC	Norway	r1i1p1f1